



1 **Causal and uncertainty-aware digital-twin framework for ultra–low-noise geoscientific inertial sensors**

2

3

4 Antonino D’Alessandro

5 Istituto Nazionale di Geofisica e Vulcanologia, Osservatorio Nazionale, Rome, Italy

6 antonino.dalessandro@ingv.it

7

8

9 **Abstract**

10 Ultra–low-noise inertial sensors are a cornerstone of modern geoscientific instrumentation, enabling high-
11 resolution observations across seismology, geodesy, gravimetry, and vibration isolation. Achieving and reliably
12 predicting their performance requires a rigorous treatment of physical causality, noise propagation, and
13 uncertainty, particularly in force-feedback architectures operating near fundamental limits. In this study, we
14 introduce a causal and uncertainty-aware digital-twin framework for the design and metrological assessment
15 of ultra–low-noise geoscientific inertial sensors. The proposed framework integrates mechanical dynamics,
16 force-feedback control, transduction, and digital acquisition within a physically realisable model that explicitly
17 enforces causality and stability constraints. Starting from a minimal equation-of-motion description, the digital
18 twin is formulated in the frequency domain to construct causal transfer functions and a comprehensive noise-
19 budget model. The framework enables the systematic separation of fundamental thermal noise limits from
20 implementation-dependent noise sources, including readout, actuation, and digital acquisition effects. We
21 introduce quantitative performance metrics based on self-noise spectra, dominant noise regimes, crossover
22 frequencies, and near-plateau bandwidths, allowing complex spectral behaviour to be condensed into
23 actionable design indicators. Parameter uncertainties are propagated through the digital twin to provide
24 uncertainty-aware performance estimates and robustness diagnostics. Through a series of illustrative analyses,
25 we demonstrate how the proposed digital twin supports informed design trade-offs, identifies performance
26 bottlenecks, and prevents non-physical or overly optimistic sensitivity estimates arising from non-causal
27 modelling assumptions. While focused on inertial sensors, the methodology is general and transferable to other



28 classes of geoscientific instruments. The framework provides a transparent and extensible foundation for next-
29 generation sensor design, virtual experimentation, and metrologically consistent performance prediction.

30

31

32 **1. Introduction**

33 The design and metrological assessment of ultra-low-noise inertial sensors for geoscientific applications
34 remains a central challenge in measurement science and engineering. These sensors — including broadband
35 seismometers, compact accelerometers, and advanced gravimetric devices (Prasad et al., 2022) — are critical
36 for resolving weak ground motions across broad frequency bands, enabling high-precision environmental
37 monitoring, earthquake early warning, and advanced observational geodesy. In practice, instrument
38 performance is constrained by a combination of fundamental thermomechanical limits and implementation-
39 dependent noise sources such as thermal (Brownian) noise of mechanical suspensions, readout electronics
40 noise, quantization error in digital acquisition, and control-loop artefacts (Ubhi et al., 2022; Zhao et al., 2022;
41 van Dongen et al., 2023).

42 Traditional sensor development has often proceeded through incremental improvements of individual
43 components, with performance characterised post-facto via laboratory calibration and field testing. While such
44 approaches are effective for benchmarking specific prototypes, they provide limited insight into the system-
45 level trade-offs between sensitivity, bandwidth, dynamic range, and robustness, particularly when uncertainty
46 propagation across the entire measurement chain is of interest. The need for rigorous uncertainty frameworks
47 in sensor design is well recognised in inertial navigation and metrology communities, where stochastic error
48 modelling and error budgeting have been emphasised (El-Sheimy et al., 2020).

49 In parallel, the concept of a digital twin has emerged as a powerful paradigm for unifying physics-based
50 simulation with real-time measurement data, enabling advanced prediction, optimisation, and uncertainty
51 quantification in complex engineered systems. Digital twin methodologies have been extensively reviewed in
52 industrial and infrastructure domains, highlighting their potential for model-based monitoring and decision
53 support (Sun et al., 2024; Carlin et al., 2024). In metrology, digital twins are gaining traction as tools for virtual
54 calibration, uncertainty evaluation, and traceability analysis across diverse measurement systems, including



55 coordinate measuring machines, optical scanners, and virtual metrological experiments (Vlaeyen et al., 2021;
56 Poroskun et al., 2022).

57 Despite these advances, the digital-twin literature remains fragmented with respect to sensor-centric, causal,
58 and uncertainty-aware frameworks that encompass both physical dynamics and digital acquisition processes.
59 Many digital twin formulations in metrology still focus on high-level concepts or specific subsystems, without
60 enforcing physical causality and realisability constraints essential for accurate modeling of closed-loop, force-
61 feedback inertial sensors. Furthermore, the representation and propagation of uncertainty through the digital
62 twin's internal variables and across the physical–digital boundary is often treated qualitatively or post hoc
63 rather than systematically (Ríos et al., 2020).

64 In the field of inertial sensing, contemporary research continues to push performance boundaries through
65 innovative mechanics and novel readout schemes, such as interferometric sensing with enhanced dynamic
66 range and low noise floors (Kranzhoff et al., 2023), as well as advanced tilt and vibration measurement systems
67 that delineate thermal and readout noise dominance across frequency (Bai et al., 2025). These efforts
68 underscore the importance of integrated noise budgeting and uncertainty analysis, yet a comprehensive, unified
69 framework that couples physical system dynamics, sensor signal chains, and digital data acquisition with
70 rigorous uncertainty propagation is still absent.

71 This manuscript addresses these gaps by introducing a causal and uncertainty-aware digital-twin framework
72 for ultra-low-noise geoscientific inertial sensors. The framework enforces physical causality and realisability
73 constraints while systematically propagating uncertainty from mechanical parameters and control elements
74 through to spectral performance metrics. It integrates mechanical modelling, transduction chains, force-
75 feedback architectures, and digital acquisition within a single, physically consistent representation (Fig. 1). By
76 decomposing self-noise into fundamental and implementation-dependent contributions and identifying
77 dominant noise regimes, the framework facilitates quantitative evaluation of design choices and metrological
78 limits.

79 Rather than relying on experimental datasets, the methodology is conceived as a design-stage tool to guide
80 sensor architecture choices and parameter selection prior to hardware realisation. The remainder of this paper
81 is organised as follows: Section 2 formalises design requirements and problem scope; Section 3 presents the
82 digital-twin architecture; Section 4 develops the comprehensive noise model; Sections 5 and 6 analyse spectral



83 performance and design trade-offs; Section 7 synthesises performance metrics and optimisation strategies;
84 Section 8 discusses broader implications and limitations; and Section 9 concludes with final remarks.

85

86

87 **2. Design requirements and problem formulation**

88 The design of ultra–low–noise inertial sensors for geoscientific applications constitutes a multi-objective
89 optimisation problem in which sensitivity, bandwidth, dynamic range, robustness, and practical
90 implementation constraints must be addressed simultaneously. Unlike post-deployment performance
91 assessment or component-level optimisation approaches, the present study formulates the sensor design
92 problem explicitly at the pre-implementation stage, adopting a system-level perspective aimed at predicting
93 achievable performance prior to hardware realisation.

94 The conceptual scope of the problem is illustrated in Fig. 1, which summarises the functional elements of a
95 force-feedback inertial sensor and their interactions. Within this framework, design requirements are not
96 treated as independent specifications but as coupled constraints that jointly define the admissible design space.

97 The primary requirement considered in this work is the attainment of ultra–low self-noise levels over a broad
98 frequency band spanning the ultra-low-frequency (ULF) regime to the classical broadband (BB) seismic band.
99 Such performance is essential for a wide range of geoscientific applications, including broadband seismology,
100 gravimetry, and long-term environmental monitoring, where weak ground motions must be resolved across
101 several decades in frequency (Collette et al., 2012; Carter et al., 2024).

102 A second key requirement concerns dynamic range and saturation behaviour. Ultra-low-noise operation must
103 coexist with the capability to accommodate large transient signals without loss of linearity, control stability, or
104 actuator authority (Sider et al., 2023). In force-feedback architectures, this requirement couples mechanical
105 design parameters, actuation strength, and control loop characteristics, precluding their independent
106 optimisation (Zhao et al., 2022).

107 Additional constraints arise from digital acquisition and system-level resources, including power consumption,
108 telemetry bandwidth, and data resolution. Finite analog-to-digital converter (ADC) resolution, clock jitter, and
109 digital signal processing limitations introduce noise contributions that may dominate the self-noise spectrum
110 over specific frequency ranges, particularly at higher frequencies. These effects must therefore be incorporated



111 explicitly into the design formulation rather than treated as secondary implementation details (El-Sheimy et
112 al., 2020; Ubezio et al., 2023).

113 Finally, the design requirements implicitly assume a set of environmental and operational conditions, including
114 mechanical coupling to the ground, thermal stability, and station infrastructure. While these factors are not
115 modelled explicitly in the present framework, they define the operating context within which the sensor is
116 expected to meet its performance objectives and delimit the interpretation of the resulting performance bounds.

117 On the basis of the above requirements, the design problem is formulated as follows: given a target sensitivity
118 spectrum, a frequency band of interest, and a set of implementation constraints, determine whether a physically
119 realisable inertial sensor architecture can achieve the desired performance and identify the dominant
120 mechanisms limiting that performance.

121 A central aspect of this formulation is the explicit separation between fundamental physical limits, such as
122 thermal noise associated with mechanical dissipation, and implementation-dependent limits arising from
123 readout electronics, actuation mechanisms, feedback control, and digital acquisition. This distinction is
124 essential for meaningful interpretation of noise budgets and for guiding design decisions toward genuinely
125 performance-limiting components rather than secondary contributors (Collette et al., 2012; Maculotti et al.,
126 2024).

127 The sensor is modelled as a linear, time-invariant system operating around a stable equilibrium point. Its
128 behaviour is described through transfer functions linking ground acceleration to the measured output quantity.
129 Nonlinear effects such as actuator saturation, hysteresis, and large-amplitude geometric nonlinearities are
130 neglected. These assumptions are standard in the analysis of ultra-low-noise inertial sensors and are justified
131 when the focus is on noise-limited performance under nominal operating conditions (Carter et al., 2024).

132 Within this framework, the observable of interest is the output acceleration estimate, whose power spectral
133 density is determined by the combined effect of the sensor dynamics and all internal noise sources propagated
134 through the system. The design objective is therefore the optimisation of the total self-noise spectrum, subject
135 to causality, stability, and realisability constraints, rather than the minimisation of individual noise sources in
136 isolation.

137 The formulation adopted here deliberately excludes experimental calibration data and site-specific noise
138 conditions. This choice reflects the intended role of the framework as a design-stage and feasibility-assessment



139 tool, rather than as a post-deployment diagnostic method. While this limits direct comparison with specific
140 instruments, it enables the identification of general trends, trade-offs, and performance bounds that are
141 transferable across sensor classes and deployment scenarios (Wright and Davidson, 2024; Ríos et al., 2020).
142 Model parameters, including mechanical damping and electronic noise levels, are assumed to be characterised
143 by probability distributions reflecting their uncertainty. The systematic propagation of these uncertainties
144 through the digital-twin framework is addressed in subsequent sections. The implications of these assumptions,
145 and their potential impact on real-world performance, are discussed in Section 8.

146

147

148 **3. Digital-twin architecture and causal modeling**

149 The digital twin developed in this study is conceived as a physics-based, causal, and uncertainty-aware
150 representation of an ultra-low-noise inertial sensor, explicitly designed to support metrological analysis and
151 design-stage optimisation. Unlike generic simulation models or reduced-order representations, the proposed
152 digital twin integrates mechanical dynamics, transduction, actuation, control, and digital acquisition within a
153 unified framework that preserves physical causality and realisability.

154 A schematic representation of the digital-twin architecture is shown in Fig. 2, which highlights the signal flow
155 from ground acceleration to the measured output through the sensor's physical and digital subsystems. This
156 architecture reflects the functional decomposition of a force-feedback inertial sensor and provides the basis for
157 subsequent noise propagation and performance analysis.

158 The mechanical subsystem is modelled as a single-degree-of-freedom inertial plant characterised by an
159 effective mass, elastic stiffness, and dissipative damping. This representation captures the dominant dynamics
160 governing the sensor response in the frequency range of interest and is commonly adopted in the analysis of
161 broadband and ultra-low-noise inertial sensors (Collette et al., 2012; Carter et al., 2024).

162 Thermal noise associated with mechanical dissipation is treated as an intrinsic property of the plant and
163 constitutes a fundamental performance limit. The mechanical model is assumed to operate in the linear regime
164 around a stable equilibrium point, and temperature is treated as a stationary parameter. Spatially distributed
165 modes, geometric nonlinearities, and thermoelastic coupling effects are neglected, an assumption justified
166 when focusing on noise-limited performance well below structural resonance frequencies.



167 The transduction stage converts the mechanical state of the plant into an electrical signal. The digital twin
168 represents this stage through a linear gain and an additive readout noise term, which may encompass optical,
169 capacitive, or electromagnetic sensing mechanisms depending on the sensor implementation. This abstraction
170 allows the framework to remain agnostic with respect to the specific readout technology while retaining its
171 metrological relevance. Compact interferometric readout implementations have recently been integrated in
172 suspended interferometers, providing practical benchmarks for low-noise readout assumptions (Carter et al.,
173 2025; Mitchell et al., 2025).

174 Readout noise is explicitly modelled as a stochastic process whose spectral characteristics can be prescribed
175 or parameterised based on design assumptions. This approach is consistent with modern inertial sensor
176 analyses, where readout noise often dominates the self-noise spectrum outside the thermal-noise-limited band
177 (Zhao et al., 2022; Carter et al., 2024).

178 Force-feedback actuation is incorporated into the digital twin to stabilise the mechanical plant and to linearise
179 the sensor response. The actuation subsystem is represented by a causal transfer function linking the control
180 signal to an applied force on the mechanical mass. Actuator noise and finite authority are treated as
181 implementation-dependent limitations and are included explicitly in the model.

182 The control architecture is described by a stabilising controller acting on the measured output. Particular care
183 is taken to ensure that the closed-loop system satisfies causality and stability constraints, as these conditions
184 directly influence noise propagation and achievable performance. Non-causal inversions or idealised feedback
185 laws are deliberately avoided, in contrast to some analytical treatments that neglect realisability constraints.

186 The final stage of the digital twin represents the digital acquisition process, including analog-to-digital
187 conversion, finite resolution, and timing uncertainty. Quantisation noise and clock jitter are modelled explicitly
188 and propagated through the system in subsequent analyses. This treatment reflects the growing recognition
189 that digital acquisition can impose dominant performance limits in ultra-low-noise sensors, particularly at
190 higher frequencies or under stringent power constraints (El-Sheimy et al., 2020; Ubezio et al., 2023).

191 Discretisation effects are treated consistently with the causal structure of the system. Continuous-time transfer
192 functions are mapped to their discrete-time counterparts using stable and physically meaningful
193 transformations. This ensures that the digital twin remains a faithful representation of a realisable sensor
194 system rather than an idealised mathematical construct. Open-source simulation toolchains widely used in



195 precision interferometry provide a reproducibility baseline for digital-twin implementations (Brown et al.,
196 2020).

197 All model parameters within the digital twin are assumed to be affected by uncertainty arising from
198 manufacturing tolerances, environmental variability, and modelling approximations. These uncertainties are
199 represented through probability distributions assigned to the relevant parameters and are propagated through
200 the digital twin in subsequent sections.

201 It is assumed that parameter uncertainties are statistically independent unless otherwise stated. While this
202 assumption may not hold in all practical cases, it provides a tractable starting point for uncertainty propagation
203 and is consistent with existing metrological digital-twin frameworks (Wright and Davidson, 2024; Maculotti
204 et al., 2024). The implications of this assumption are discussed in Section 8.

205 Within the proposed digital-twin framework, the mechanical plant and the force-feedback actuation are
206 compactly described by the equation of motion

207

$$208 \quad m \ddot{x}(t) + c \dot{x}(t) + k x(t) = - m a_g(t) + F_{fb}(t), \quad (1)$$

209

210 where $x(t)$ denotes the relative displacement of the inertial mass with respect to the sensor frame, $a_g(t)$ is the
211 ground acceleration to be measured, m , c , and k represent the effective mass, damping coefficient, and stiffness
212 of the mechanical plant, and $F_{fb}(t)$ is the feedback force applied by the actuator. Equation (1) provides the
213 physical backbone of the digital twin, from which the causal transfer functions and noise propagation
214 relationships are derived in the frequency domain in the following section.

215

216

217 **4. Metrological noise modeling and uncertainty propagation**

218 The metrological performance of an ultra-low-noise inertial sensor is ultimately determined by the propagation
219 of multiple stochastic noise sources through the causal dynamics of the sensor system. Building on the physical
220 model introduced in Section 3, this section formalises the noise modeling framework adopted in the digital
221 twin and defines the methodology used to propagate uncertainty from individual noise sources to the total self-
222 noise spectrum.



223 A schematic overview of the noise budget and its decomposition into individual contributions is shown in Fig.
224 3, which provides a graphical representation of the formalism developed below.
225 Starting from the equation of motion introduced in Eq. (1), the system is transformed into the frequency domain
226 under the assumption of linear, time-invariant dynamics. Denoting Fourier-transformed quantities by capital
227 letters, the relative displacement $X(\omega)$ of the inertial mass can be written as

228

$$230 \quad X(\omega) = \frac{-m A_g(\omega) + F_{fb}(\omega)}{k - m\omega^2 + ic\omega}, \quad (2)$$

229

231 where $A_g(\omega)$ is the ground acceleration spectrum and $F_{fb}(\omega)$ represents the feedback force in the frequency
232 domain. Equation (2) defines the mechanical susceptibility of the plant and provides the basis for constructing
233 the transfer functions linking each noise source to the sensor output.

234 In a force-feedback configuration, the measured output is typically proportional to an estimate of the ground
235 acceleration derived from the control signal and the plant response. The digital twin represents this relationship
236 through a set of causal transfer functions $T_q(\omega)$, each associated with a specific noise source q .

237 The total self-noise of the sensor is defined as the output noise spectrum obtained in the absence of ground
238 motion, i.e. for $A_g(\omega) = 0$. Under this condition, the output acceleration noise power spectral density (PSD)
239 can be expressed as the incoherent sum of the contributions from all internal noise sources,

240

$$242 \quad S_{a,\text{self}}(\omega) = \sum_q |T_q(\omega)|^2 S_q(\omega), \quad (3)$$

241

243 where $S_q(\omega)$ denotes the PSD of the q -th noise source and $T_q(\omega)$ is the corresponding transfer function from
244 that source to the output acceleration estimate. Equation (3) constitutes the central metrological relation of the
245 framework and formalises the noise-budget decomposition illustrated in Fig. 3.

246 The noise sources considered in this work include: (i) thermal (Brownian) noise associated with mechanical
247 dissipation, (ii) readout noise originating from the transduction stage, (iii) actuation noise introduced by the
248 force-feedback mechanism, (iv) digital acquisition noise, including quantisation and timing uncertainty.



249 Thermal noise associated with mechanical damping represents a fundamental physical limit that cannot be
250 reduced without modifying the underlying dissipation mechanisms. Its contribution is governed by the
251 fluctuation–dissipation theorem and depends on temperature, damping, and mechanical susceptibility (Collette
252 et al., 2012).

253 In contrast, readout, actuation, and digital acquisition noises are implementation-dependent and reflect
254 technological and design choices. Their relative importance varies across frequency and design parameter
255 space, and they often dominate the self-noise spectrum outside the thermal-noise-limited band (Zhao et al.,
256 2022; Carter et al., 2024). The explicit separation between these two classes of noise sources is essential for
257 interpreting metrological bounds and guiding effective design optimisation.

258 All noise sources and model parameters entering Eq. (3) are subject to uncertainty arising from manufacturing
259 tolerances, environmental variability, and modelling assumptions. Within the digital-twin framework, these
260 uncertainties are represented through probability distributions assigned to the relevant parameters.

261 Uncertainty propagation is performed by evaluating the statistical distribution of the self-noise spectrum
262 resulting from Eq. (3), given the distributions of $S_q(\omega)$ and the parameters defining $T_q(\omega)$. This approach
263 enables the estimation of confidence intervals on the predicted self-noise and provides a quantitative measure
264 of robustness with respect to parameter variability, in line with modern metrological digital-twin concepts
265 (Scholz et al., 2022; Wübbeler et al., 2022; Wright and Davidson, 2024; Maculotti et al., 2024).

266 Parameter correlations are neglected unless explicitly stated. While this assumption may not hold in all
267 practical implementations, it allows the identification of dominant uncertainty drivers and represents a
268 reasonable first-order approximation for design-stage analysis.

269 The noise modeling framework assumes linearity, stationarity, and mutual incoherence of the noise sources.
270 Cross-correlations between noise processes and non-stationary effects are not considered. These assumptions
271 are standard in inertial sensor metrology and are justified when the objective is to characterise noise-limited
272 performance under nominal operating conditions.

273 The implications of these assumptions, and their potential impact on real-world sensor behaviour, are discussed
274 in Section 8.

275

276



277 5. Spectral performance and self-noise regimes

278 This section analyses the spectral performance predicted by the digital twin and characterises the resulting self-
279 noise in terms of dominant noise regimes across frequency. The objective is to translate the metrological
280 formulation introduced in Section 4 into physically interpretable performance metrics that are directly relevant
281 for sensor design.

282 A representative example of the self-noise spectrum and its decomposition into individual contributions is
283 shown in Fig. 4, which illustrates how fundamental and implementation-dependent noise sources shape the
284 achievable performance across the frequency band of interest.

285 The total self-noise spectrum $S_{a,\text{self}}(\omega)$, defined in Eq. (3), typically exhibits distinct frequency-dependent
286 behaviours governed by the interplay between mechanical susceptibility and noise transfer functions. Of
287 particular interest is the presence of noise plateaus, i.e. frequency intervals over which the self-noise remains
288 approximately constant.

289 To formalise this concept, the acceleration self-noise amplitude spectral density (ASD) is defined as

290

$$292 N_a(\omega) = \sqrt{S_{a,\text{self}}(\omega)}. \quad (4)$$

291

293 A plateau region is identified when the logarithmic slope of $N_a(\omega)$ with respect to frequency satisfies

294

$$296 \left| \frac{d \log N_a(\omega)}{d \log \omega} \right| < \varepsilon, \quad (5)$$

295

297 where ε is a small threshold chosen to discriminate between flat and sloped spectral behaviour. While the
298 precise value of ε is application-dependent, the qualitative identification of plateau regions is robust with
299 respect to reasonable threshold variations.

300 Plateaus are of particular metrological relevance because they define frequency bands in which the sensor
301 sensitivity is maximised and least sensitive to modelling uncertainties.

302 Across the full frequency band, different noise sources dominate the self-noise spectrum. At low frequencies,
303 the response is typically governed by thermal noise associated with mechanical damping, reflecting the



304 fundamental limit imposed by dissipation mechanisms. In intermediate frequency ranges, readout or actuation
305 noise may dominate, depending on the chosen transduction and control architecture. At higher frequencies,
306 digital acquisition noise, including quantisation and timing uncertainty, often becomes the limiting factor.
307 These dominant noise regimes are identified by comparing the individual terms in Eq. (3) and determining, at
308 each frequency, the noise source contributing the largest fraction to $S_{a,\text{self}}(\omega)$. This regime-based interpretation
309 is illustrated in Fig. 4, where transitions between thermal-limited and implementation-limited behaviour are
310 clearly visible.

311 The identification of dominant regimes is a consolidated result, as it directly follows from the noise budget
312 formalism and does not depend on subjective interpretation. In contrast, the precise frequency boundaries
313 between regimes should be regarded as model-dependent and may shift as design parameters or uncertainty
314 assumptions are varied.

315 A central outcome of the spectral analysis is the explicit comparison between the total self-noise and the
316 thermal noise floor. The ratio

317

$$318 \quad R(\omega) = \frac{S_{a,\text{self}}(\omega)}{S_{a,\text{th}}(\omega)} \quad (6)$$

318

320 provides a frequency-dependent measure of the margin to the thermal limit, where $S_{a,\text{th}}(\omega)$ denotes the thermal
321 noise contribution. Values of $R(\omega)$ close to unity indicate near-thermal-limited performance, whereas larger
322 values highlight the dominance of implementation-dependent noise sources.

323 This ratio constitutes a key diagnostic metric for sensor design, as it directly indicates whether further
324 performance improvements require fundamental changes to the mechanical plant or, alternatively,
325 technological improvements in readout, actuation, or digital acquisition. The interpretation of $R(\omega)$ across
326 frequency is illustrated in Fig. 4, where near-thermal and implementation-limited bands can be clearly
327 distinguished.

328 The spectral features identified in this section are a direct consequence of the causal structure of the digital
329 twin and the noise modeling assumptions introduced in Section 4. While the existence of plateaus and dominant



330 noise regimes is a robust qualitative result, their quantitative characteristics depend on model parameters and
331 uncertainty distributions.

332 Nonlinear effects, cross-correlations between noise sources, and non-stationary behaviour are not considered
333 in this analysis. These factors may alter the detailed spectral structure in real instruments, particularly under
334 extreme operating conditions. Nevertheless, the regime-based interpretation presented here provides a
335 physically meaningful and practically useful framework for guiding sensor design.

336

337

338 **6. Crossover frequencies and design trade-offs**

339 While the identification of dominant noise regimes provides a qualitative understanding of sensor performance,
340 practical design decisions require quantitative metrics capable of capturing transitions between regimes and
341 their dependence on key design parameters. In this section, such metrics are introduced through the concept of
342 crossover frequencies, which mark the boundaries between noise-dominated regimes and provide a compact
343 description of performance trade-offs.

344 A representative mapping of crossover frequencies and dominant regimes in the design parameter space is
345 shown in Fig. 6, which synthesises the spectral analyses discussed in the previous section.

346 For any pair of noise sources q_1 and q_2 , a crossover frequency $\omega_c^{(q_1, q_2)}$ is defined as the solution of

347

$$348 \quad |T_{q_1}(\omega_c)|^2 S_{q_1}(\omega_c) = |T_{q_2}(\omega_c)|^2 S_{q_2}(\omega_c), \quad (7)$$

349

350 i.e. the frequency at which the contributions of the two noise sources to the total self-noise spectrum are equal.

351 Below and above this frequency, the dominant contribution switches from one noise source to the other.

352 In practice, the most relevant crossover frequencies involve transitions between thermal noise and
353 implementation-dependent noise sources, such as readout or digital acquisition noise. These transitions
354 delineate frequency intervals in which further performance improvements require fundamentally different
355 design strategies.



356 Building on the plateau definition introduced in Section 5, the near-plateau bandwidth is defined as the
357 frequency interval over which the self-noise remains within a prescribed margin of the minimum achievable
358 level. Formally, this interval is given by

359

$$361 \quad N_a(\omega) \leq (1 + \delta) N_{a,\min}, \quad (8)$$

360

362 where $N_{a,\min}$ is the minimum value of the self-noise ASD and δ is a tolerance parameter. The near-plateau
363 bandwidth provides a concise metric for assessing the usable frequency range over which the sensor operates
364 close to its optimal sensitivity.

365 As illustrated in Fig. 6, this bandwidth is strongly dependent on implementation parameters such as ADC
366 resolution and control-loop design, and it often represents a more informative performance metric than the
367 absolute minimum noise level alone.

368 The crossover frequencies and near-plateau bandwidth jointly define a design trade-off space in which
369 improvements along one dimension may degrade performance along another. For example, increasing digital
370 resolution can extend the near-plateau bandwidth toward higher frequencies but may impose penalties in power
371 consumption or system complexity. Conversely, modifying mechanical damping may shift thermal-to-readout
372 crossover frequencies at the expense of increased sensitivity to environmental perturbations.

373 The regime maps shown in Fig. 6 summarise these trade-offs by identifying, for each region of the parameter
374 space, the noise source that ultimately limits performance. These maps constitute a consolidated result, as they
375 are derived directly from the noise-budget formalism and the causal structure of the digital twin. However, the
376 precise boundaries between regimes should be interpreted as model-dependent, reflecting assumptions on
377 parameter uncertainty and noise spectra.

378 From a design perspective, crossover-based metrics provide actionable guidance by indicating whether further
379 optimisation efforts should focus on fundamental mechanical improvements or on technological enhancements
380 in readout, actuation, or digital acquisition. In this sense, crossover frequencies act as decision thresholds
381 separating regimes where different design strategies are effective.

382 It is important to note that crossover frequencies are not intrinsic properties of the sensor but emerge from the
383 interaction between physical dynamics and implementation choices. As such, they should be interpreted within



384 the context of the assumed operating conditions and uncertainty model. The broader implications of this
385 dependence are discussed in Section 8.

386

387

388 **7. Performance metrics and design optimization**

389 The spectral analyses and crossover-based diagnostics introduced in the previous sections provide detailed
390 insight into the noise-limited behaviour of ultra-low-noise inertial sensors. For design purposes, however, it is
391 often desirable to condense this information into a limited set of performance metrics that can guide
392 optimisation decisions and enable comparisons between alternative architectures. This section introduces such
393 metrics and illustrates their role within the digital-twin framework.

394 A synthesis of the performance metrics discussed below and their dependence on key design parameters is
395 shown in Fig. 7, which summarises the design space explored in this study.

396 A primary metric is the minimum self-noise level, defined as

397

$$399 \quad N_{a,\min} = \min_{\omega} N_a(\omega), \quad (9)$$

398

400 where $N_a(\omega)$ is the self-noise ASD defined in Eq. (4). While $N_{a,\min}$ provides a compact measure of ultimate
401 sensitivity, it does not capture the frequency extent over which this sensitivity is achieved. As such, it should
402 not be used in isolation to rank sensor designs.

403 Complementary information is provided by the near-plateau bandwidth introduced in Section 6, which
404 quantifies the usable frequency interval over which the self-noise remains close to its minimum value.

405 Together, these two metrics define a sensitivity–bandwidth trade-off that is central to sensor design.

406 To assess how closely a given design approaches the fundamental thermal noise limit, the margin to the thermal
407 bound is evaluated using the ratio defined in Eq. (6). For practical design optimisation, a scalar metric can be
408 introduced by averaging this ratio over a frequency interval of interest $[\omega_1, \omega_2]$,

409

$$410 \quad \bar{R} = \frac{1}{\omega_2 - \omega_1} \int_{\omega_1}^{\omega_2} \frac{S_{a,\text{self}}(\omega)}{S_{a,\text{th}}(\omega)} d\omega. \quad (10)$$



411

412 Values of \bar{R} close to unity indicate near-thermal-limited performance over the selected band, whereas larger
413 values highlight the dominance of implementation-dependent noise sources. This metric is particularly useful
414 for identifying whether further optimisation efforts should focus on mechanical design or on technological
415 improvements in readout and digital acquisition.

416 Beyond absolute performance, robustness with respect to parameter uncertainty constitutes a critical aspect of
417 sensor design. Within the digital-twin framework, robustness is assessed by analysing the variability of the
418 performance metrics introduced above under the assumed parameter uncertainty distributions.

419 Designs that achieve marginally lower self-noise but exhibit strong sensitivity to parameter variations may be
420 less desirable than slightly noisier but more robust configurations. This consideration is especially relevant for
421 long-term geoscientific deployments, where environmental variability and ageing effects can significantly
422 impact performance (Wright and Davidson, 2024).

423 The optimisation strategy adopted here therefore prioritises uncertainty-aware performance, favouring regions
424 of the design space in which sensitivity, bandwidth, and robustness are jointly optimised. The regime maps
425 shown in Fig. 7 illustrate how such regions can be identified and compared across alternative design choices.

426 Within the proposed framework, design optimisation proceeds iteratively. Initial design choices define a
427 candidate digital twin, whose performance metrics are evaluated using the methods described above. Identified
428 bottlenecks then guide targeted modifications to mechanical parameters, control architecture, or digital
429 acquisition settings, and the analysis is repeated until the desired performance objectives are met.

430 This optimisation process is methodologically consolidated, as it relies on physically interpretable metrics
431 derived directly from the causal digital twin. At the same time, specific optimisation outcomes remain context-
432 dependent, reflecting application-specific requirements and constraints. The broader implications of this
433 balance between generality and specificity are discussed in Section 8.

434

435

436 **8. Discussion**

437 This section discusses the implications of the proposed causal and uncertainty-aware digital-twin framework,
438 placing the results presented in Sections 4–7 in a broader methodological and instrumental context. The



439 discussion focuses on the generality of the approach, its limitations, and its relevance for the design of ultra-
440 low-noise geoscientific inertial sensors.

441 A conceptual synthesis of the workflow and its role in guiding design decisions is illustrated in Fig. 8, which
442 integrates the individual analysis steps into a unified methodological framework.

443 A key outcome of this study is the demonstration that enforcing physical causality and realisability constraints
444 at the digital-twin level is essential for obtaining meaningful metrological predictions. Non-causal inversions
445 or idealised feedback representations, while mathematically convenient, can lead to overly optimistic noise
446 estimates and obscure the distinction between fundamental and implementation-dependent limits.

447 By explicitly modelling the force-feedback loop as a causal subsystem, the present framework ensures that
448 noise propagation remains physically interpretable across all frequency bands. This feature represents a
449 consolidated methodological result and aligns with recent metrological perspectives that emphasise the need
450 for trustworthy virtual experiments grounded in physical realism (Wright and Davidson, 2024; Maculotti et
451 al., 2024).

452 The performance metrics introduced in Sections 6 and 7 provide a compact representation of complex spectral
453 information and facilitate comparison between alternative sensor architectures. In particular, crossover
454 frequencies and near-plateau bandwidths offer actionable indicators of where design effort is most effectively
455 directed.

456 The regime maps derived from these metrics should be interpreted as decision-support tools rather than as
457 absolute performance predictors. While the existence of distinct noise-dominated regimes is a robust outcome
458 of the noise-budget formalism, the precise boundaries between regimes depend on modelling assumptions and
459 uncertainty characterisation. This sensitivity underscores the importance of uncertainty-aware optimisation
460 strategies in sensor design.

461 Although the digital twin is formulated with force-feedback inertial sensors in mind, the underlying
462 methodology is not restricted to a specific sensor type. The same framework can be adapted to other classes of
463 geoscientific instruments, such as tiltmeters, gravimeters, or strain sensors, including atom-interferometry
464 gravimeters demonstrated in harsh volcanic environments (Antoni-Micollier et al., 2022), provided that their
465 dynamics can be represented within a linear, causal system framework.



466 The abstraction of transduction, actuation, and digital acquisition as modular subsystems facilitates such
467 extensions and supports the development of sensor-specific digital twins within a common metrological
468 structure. This generality is consistent with recent efforts to standardise digital-twin methodologies across
469 measurement domains (Ríos et al., 2020; Ubezio et al., 2023).

470 Several limitations of the present framework should be acknowledged. First, the analysis assumes linearity,
471 stationarity, and mutual incoherence of noise sources. While these assumptions are standard in inertial sensor
472 metrology, they may be violated under extreme operating conditions or in the presence of strong environmental
473 coupling.

474 Second, parameter uncertainties are treated as statistically independent unless explicitly stated. In real
475 instruments, correlations between mechanical, electronic, and environmental parameters may exist and could
476 affect uncertainty propagation. Incorporating such correlations would require additional modelling effort and
477 data, which lies beyond the scope of the present study.

478 Finally, the framework does not incorporate site-specific noise conditions or experimental calibration data. As
479 a result, the predicted performance should be interpreted as an intrinsic sensor capability rather than as a
480 guarantee of field performance. This distinction is particularly important when comparing digital-twin
481 predictions with observational data.

482 Despite these limitations, the proposed framework provides a solid foundation for future extensions. Potential
483 developments include the incorporation of nonlinear effects, the integration of experimental calibration data
484 to refine parameter distributions, and the coupling of the digital twin with real-time monitoring systems. Data-
485 driven denoising approaches have also been explored for inertial sensors/accelerometers and may complement
486 model-based digital twins (Yang et al., 2023).

487 Such extensions would further enhance the utility of digital twins as tools for both design-stage optimisation
488 and operational performance assessment in geoscientific instrumentation.

489

490

491 **9. Conclusions**

492 This work introduces a causal and uncertainty-aware digital-twin framework for the design and metrological
493 assessment of ultra-low-noise geoscientific inertial sensors. The proposed approach integrates mechanical



494 dynamics, force-feedback control, transduction, and digital acquisition within a unified, physically realisable
495 model, explicitly enforcing causality and stability constraints throughout the analysis.

496 A central result of this study is the formulation of a metrologically consistent noise-budget framework that
497 enables the propagation of multiple stochastic noise sources to the sensor output while preserving their physical
498 interpretation. By distinguishing between fundamental thermal limits and implementation-dependent noise
499 contributions, the digital twin provides a transparent basis for interpreting self-noise spectra and identifying
500 dominant noise regimes across frequency.

501 The introduction of crossover frequencies, near-plateau bandwidths, and uncertainty-aware performance
502 metrics represents a further consolidated contribution. These quantities condense complex spectral information
503 into actionable indicators that support design-stage optimisation and facilitate objective comparisons between
504 alternative sensor architectures. Importantly, the framework highlights that proximity to fundamental limits is
505 inherently frequency-dependent and strongly influenced by implementation choices.

506 From a methodological perspective, this work demonstrates that enforcing causality and realisability at the
507 digital-twin level is not merely a formal requirement but a necessary condition for obtaining trustworthy
508 performance predictions. The results show that non-causal or idealised representations can obscure critical
509 trade-offs and lead to overly optimistic sensitivity estimates, particularly in ultra-low-noise regimes.

510 Several limitations of the present study should be acknowledged. The analysis is restricted to linear, stationary
511 behaviour and assumes mutual incoherence of noise sources, as well as statistically independent parameter
512 uncertainties. Moreover, the framework intentionally focuses on intrinsic sensor capabilities and does not
513 incorporate site-specific environmental noise or experimental calibration data. These aspects should be
514 considered when comparing digital-twin predictions with field observations.

515 Despite these limitations, the proposed framework provides a robust and extensible foundation for future
516 developments. Potential extensions include the incorporation of nonlinear effects, correlated uncertainties,
517 experimental calibration data, and real-time data assimilation. Beyond inertial sensors, the methodology is
518 readily transferable to other classes of geoscientific instruments, supporting the broader adoption of digital
519 twins as design and decision-support tools in geoscientific instrumentation.



520 In summary, this study establishes a rigorous, transparent, and generalisable digital-twin framework that
521 bridges physical modelling, metrological analysis, and uncertainty-aware design optimisation, offering a
522 concrete pathway toward the development of next-generation ultra-low-noise geoscientific sensors.

523

524

525 **Competing interests:**

526 The authors declare that they have no conflict of interest

527

528

529 **10. References**

530 Antoni-Micollier, L., *et al.* (2022). Detecting volcano-related underground mass changes with a quantum
531 gravimeter. *Geophysical Research Letters*, 49, e2022GL097814. <https://doi.org/10.1029/2022GL097814>

532

533 Bai, W., Feng, W., Wang, P., Zhang, Z., and Zhao, G. (2025). Research on Interferometric Tilt Sensor for
534 Vibration Isolation Platform. *Sensors*, 25(6), 1777. <https://doi.org/10.3390/s25061777>

535

536 Brown, D. D., Jones, P., Rowlinson, S., Leavey, S., Green, A. C., Töyrä, D., and Freise, A. (2020). Pykat:
537 Python package for modelling precision optical interferometers. *SoftwareX*, 12, 100613.
538 <https://doi.org/10.1016/j.softx.2020.100613>

539

540 Carlin, *et al.* (2024). An interactive framework to support decision-making for Digital Twin design. *Journal of*
541 *Industrial Information Integration*, 41, 100639. <https://doi.org/10.1016/j.jii.2024.100639>

542

543 Carter, J. J., Birckigt, P., Gerberding, O., and Koehlenbeck, S. M. (2024). High precision inertial sensors on a
544 one inch diameter optic. *Scientific Reports*, 14. <https://doi.org/10.1038/s41598-024-68623-0>

545



- 546 Carter, J. J., *et al.* (2025). Testing compact, fused silica resonator based inertial sensors in a gravitational wave
547 detector prototype facility. *Classical and Quantum Gravity*, 42(18), 185001. <https://doi.org/10.1088/1361->
548 6382/adff34
- 549
- 550 Collette, C., Janssens, S., Fernandez-Carmona, P., Artoos, K., Guinchar, M., Hauviller, C., and Preumont, A.
551 (2012). Review: Inertial sensors for low-frequency seismic vibration measurement. *Bulletin of the*
552 *Seismological Society of America*, 102(4), 1289–1300. <https://doi.org/10.1785/0120110223>
- 553
- 554 El-Sheimy, N., Yoon, S., and Jiang, Z. (2020). Inertial sensors technologies and error modelling for navigation
555 and uncertainty analysis. *Journal of Applied Geodesy*, 14(2), 115–134. <https://doi.org/10.1186/s43020-019->
556 0001-5
- 557
- 558 Kranzhoff, S. L., Lehmann, J., Kirchhoff, R., *et al.* (2023). A vertical inertial sensor with interferometric
559 readout. *Classical and Quantum Gravity*, 40(1), 015007. <https://doi.org/10.1088/1361-6382/aca45b>
- 560
- 561 Maculotti, G., Elster, C., Wübbeler, G., *et al.* (2024). A shared metrological framework for trustworthy virtual
562 experiments and digital twins. *Metrology*, 4(3), 337–363. <https://doi.org/10.3390/metrology4030021>
- 563
- 564 Mitchell, A., *et al.* (2025). Integration of high-performance compact interferometric sensors in a suspended
565 interferometer. *Classical and Quantum Gravity*, 42(19), 195014. <https://doi.org/10.1088/1361-6382/ae0087>
- 566
- 567 Poroskun, I., Rothleitner, C., and Heißelmann, D. (2022). Structure of digital metrological twins as software
568 for uncertainty estimation. *Journal of Sensors and Sensor Systems*, 11, 75–82. <https://doi.org/10.5194/jsss-11->
569 75-2022
- 570
- 571 Prasad, A., Middlemiss, R. P., Noack, A., *et al.* (2022). A 19 day earth tide measurement with a MEMS
572 gravimeter. *Scientific Reports*, 12, 13091. <https://doi.org/10.1038/s41598-022-16881-1>



573

574 Ríos, J., Staudter, G., Weber, M., and Anderl, R. (2020). Uncertainty of data and the digital twin: a review.

575 *International Journal of Product Lifecycle Management*, 12(4), 329–358.

576 <https://doi.org/10.1504/IJPLM.2020.10035102>

577

578 Scholz, G., Fortmeier, I., Marschall, M., et al. (2022). Experimental design for virtual experiments in tilted-
579 wave interferometry. *Metrology*, 2(1), 84–97. <https://doi.org/10.3390/metrology2010006>

580

581 Sider, A., Di Fronzo, C., Amez-Droz, L., et al. (2023). E-TEST: a compact low-frequency isolator for a large
582 cryogenic mirror. *Classical and Quantum Gravity*, 40(16), 165002. <https://doi.org/10.1088/1361-6382/ace230>

583

584 Sun, Z., Wang, Q., Pan, J., et al. (2024). Review on digital twin applications and development challenges in
585 structural monitoring. *Sensors*, 25(1), 59. <https://doi.org/10.3390/s25010059>

586

587 Ubezio, B., Ergun, S., and Zangl, H. (2023). Realistic sensor simulations for the digital twin.
588 *e+i Elektrotechnik und Informationstechnik*, 140(10), 562–571. <https://doi.org/10.1007/s00502-023-01156-y>

589

590 Ubhi, A. S., Prokhorov, L., Cooper, S., et al. (2022). Active platform stabilization with a 6D seismometer.
591 *Applied Physics Letters*, 121, 174101. <https://doi.org/10.1063/5.0118606>

592

593 van Dongen, J., et al. (2023). Reducing control noise in gravitational wave detectors with interferometric local
594 damping of suspended optics. *Review of Scientific Instruments*, 94(5), 054501.

595 <https://doi.org/10.1063/5.0144865>

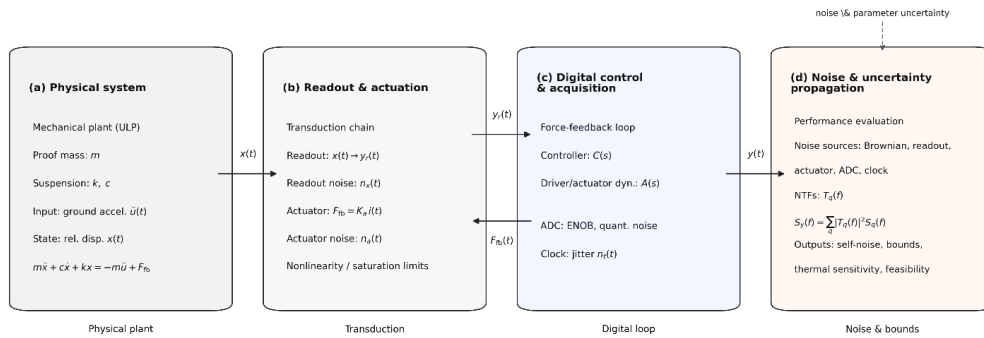
596

597 Vlaeyen, M., et al. (2021). Digital twin of an optical measurement system.
598 *Sensors*, 21(19), 6638. <https://doi.org/10.3390/s21196638>

599

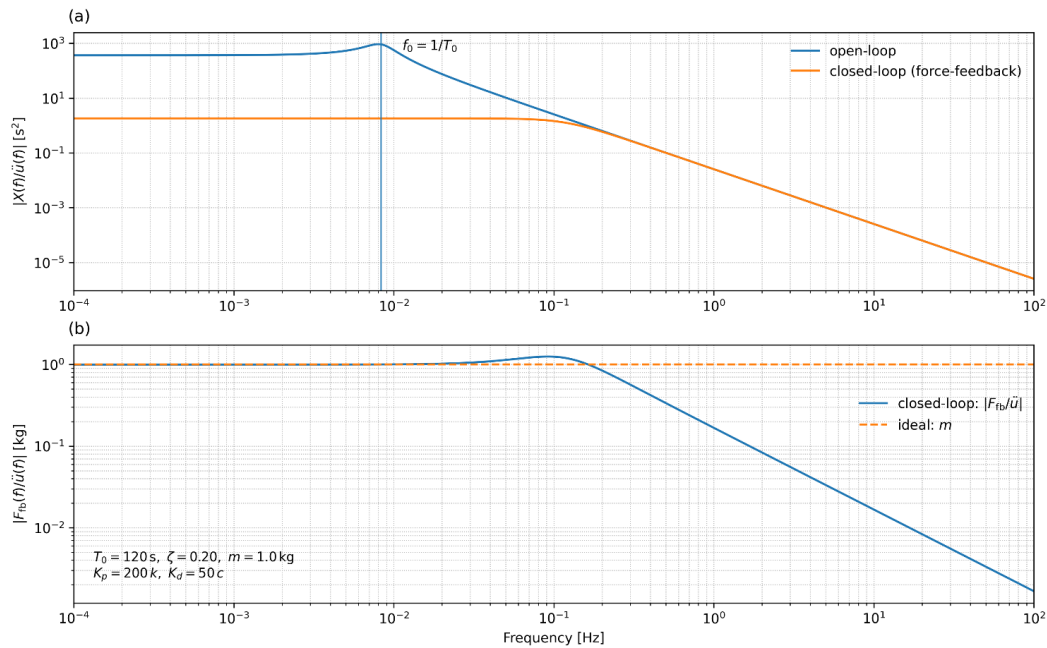


- 600 Wright, L., and Davidson, S. (2024). Digital twins for metrology; metrology for digital twins.
601 *Measurement Science and Technology*, 35. <https://doi.org/10.1088/1361-6501/ad2050>
602
- 603 Wübbeler, G., Marschall, M., Kniel, K., Heißelmann, D., Härtig, F., and Elster, C. (2022). GUM-Compliant
604 Uncertainty Evaluation Using Virtual Experiments. *Metrology*, 2(1), 114–127.
605 <https://doi.org/10.3390/metrology201000>
606
- 607 Zhao, G., et al. (2022). An interferometric inertial sensor for low-frequency seismic isolation.
608 *Sensors and Actuators A: Physical*, 335, 113398. <https://doi.org/10.1016/j.sna.2022.113398>
609
- 610 Yang, Z., Zhang, H., Xu, P., and Luo, Z. (2023). Unsupervised Noise Reductions for Gravitational Reference
611 Sensors or Accelerometers Based on the Noise2Noise Method. *Sensors*, 23(13), 6030.
612 <https://doi.org/10.3390/s23136030>



613

614 **Figure 1.** Conceptual block diagram of the digital-twin framework adopted for the analysis and design of a
 615 force-feedback ultra-long-period (ULP) seismometer. (a) Physical system: mechanical plant modeled as a
 616 proof mass–spring–damper system, driven by ground acceleration and controlled via feedback force, described
 617 by the equation of motion $m\ddot{x} + c\dot{x} + kx = -m\ddot{u} + F_{fb}$. (b) Readout and actuation: transduction chain
 618 mapping the relative displacement $x(t)$ into the readout signal $y_r(t)$, including readout noise and actuator
 619 dynamics, force generation, and nonlinearity or saturation effects. (c) Digital control and acquisition: closed-
 620 loop force-feedback architecture comprising the digital controller $C(s)$, driver/actuator dynamics $A(s)$,
 621 analog-to-digital conversion (ENOB and quantization noise), and clock jitter; yielding the output signal $y(t)$ in
 622 physical units. (d) Noise and uncertainty propagation: evaluation of the contribution of independent noise
 623 sources (Brownian, readout, actuator, ADC, and clock) through their corresponding noise transfer functions
 624 $T_q(f)$, resulting in the output power spectral density $S_y(f) = \sum_q |T_q(f)|^2 S_q(f)$. The framework enables
 625 quantitative assessment of self-noise, theoretical performance bounds, thermal sensitivity, and overall
 626 feasibility of the instrument design.



627

628 **Figure 2.** Frequency-domain response of the ultra-long-period (ULP) force-feedback seismometer digital twin.

629 (a) Magnitude of the mechanical compliance $|X(f)/\ddot{u}(f)|$, comparing the open-loop response of the

630 mechanical plant with the closed-loop response obtained through force-feedback control. The open-loop

631 resonance at the natural frequency $f_0 = 1/T_0$ is clearly visible, while the closed-loop configuration suppresses

632 the resonance and significantly reduces proof-mass motion over a broad frequency band. (b) Magnitude of the

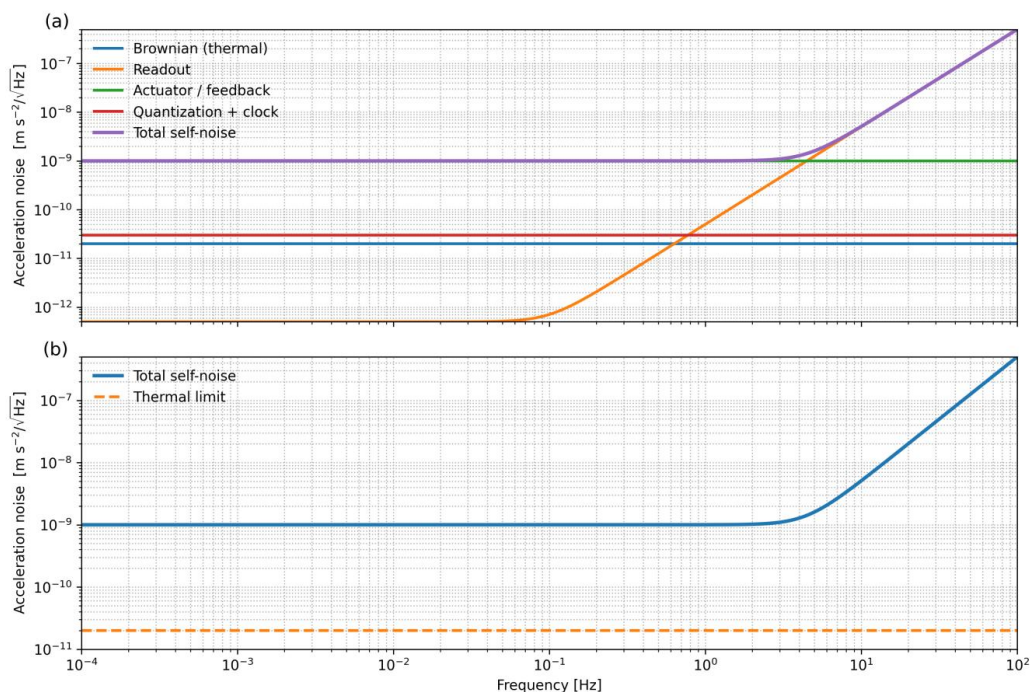
633 force-balance transfer function $|F_{fb}(f)/\ddot{u}(f)|$ in the closed-loop configuration, compared with the ideal low-

634 frequency limit $F_{fb}/\ddot{u} = m$. At low frequencies, the feedback force accurately tracks the inertial force

635 associated with ground acceleration, whereas at higher frequencies the response rolls off due to the finite

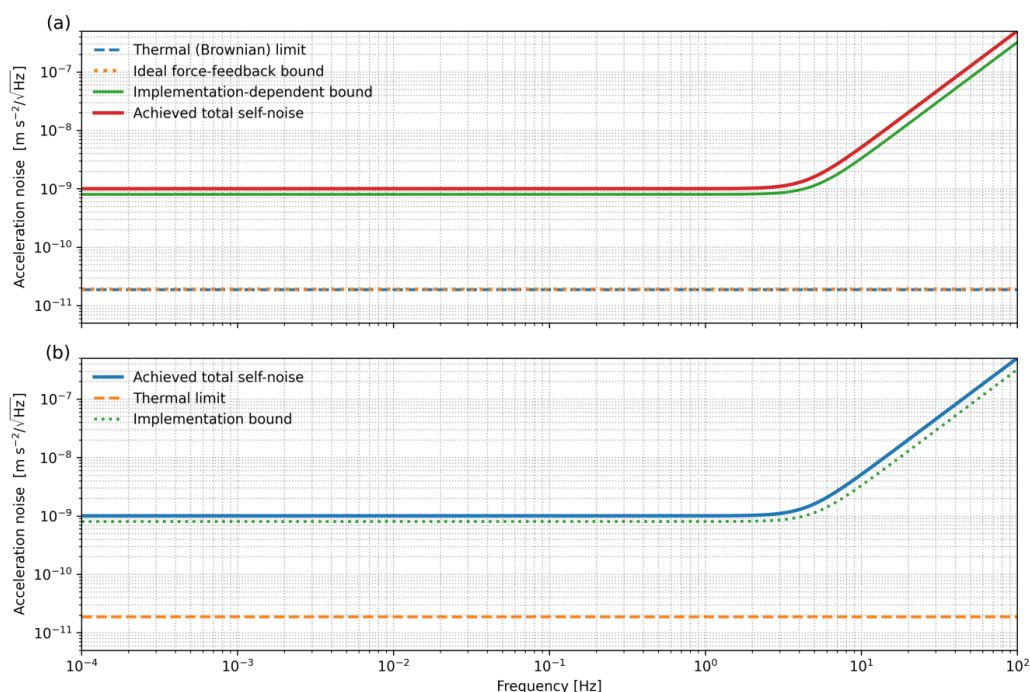
636 bandwidth of the control loop. The parameters reported in the inset correspond to a representative ULP

637 configuration and a proportional–derivative feedback law.



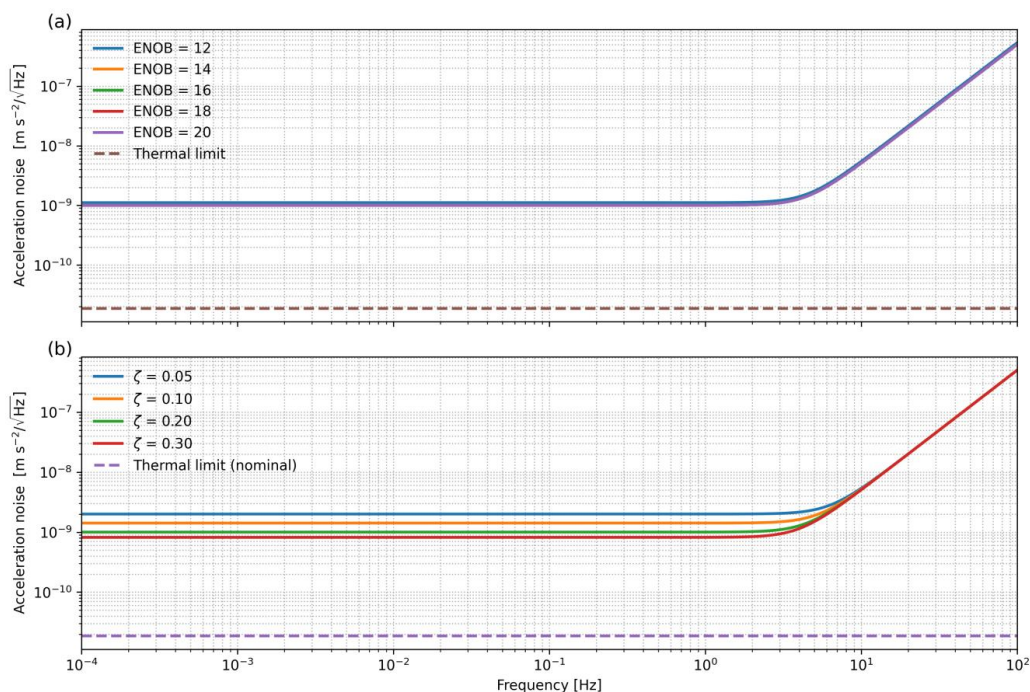
638

639 **Figure 3.** Frequency-dependent acceleration self-noise budget of the force-feedback ULP seismometer derived
640 from the digital-twin framework. (a) Individual noise contributions referred to input acceleration, including
641 Brownian (thermal) noise of the mechanical plant, readout noise, actuator/feedback noise, and quantization
642 plus clock jitter, together with their quadratic sum defining the total self-noise. The spectrum highlights the
643 transition from readout- and quantization-limited performance at low frequencies to feedback- and control-
644 limited behavior at higher frequencies. (b) Comparison between the total self-noise and the fundamental
645 thermal limit set by the mechanical suspension. Model parameters are indicated in the panel and correspond
646 to a nominal ultra-long-period design with force-feedback control. The separation between the total self-noise
647 and the thermal limit quantifies the residual performance gap attributable to non-thermal noise sources and
648 control-loop implementation.



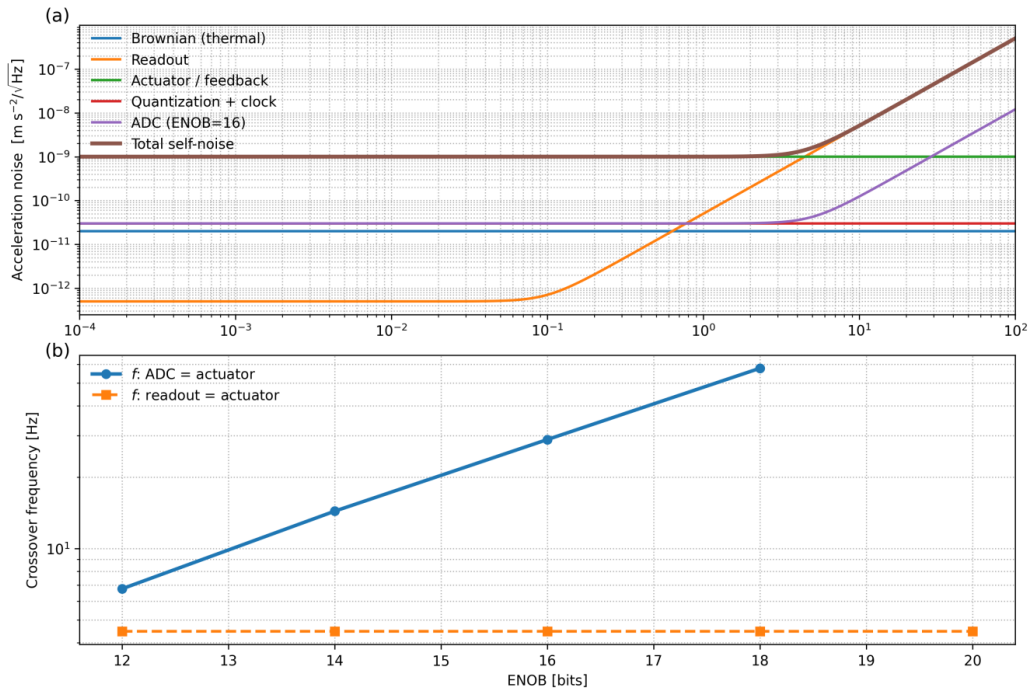
649

650 **Figure 4.** Metrological acceleration-noise bounds and achieved performance of the force-feedback ultra-long-
651 period (ULP) seismometer derived from the digital-twin framework. (a) Fundamental and implementation-
652 dependent noise bounds referred to input acceleration. The thermal (Brownian) limit represents the irreducible
653 noise floor imposed by mechanical dissipation in the suspension. The ideal force-feedback bound coincides
654 with the thermal limit in the absence of electronic and control noise and is shown with a slight offset for visual
655 clarity. The implementation-dependent bound accounts for practical non-idealities introduced by actuation,
656 digitization, timing, and control-loop dynamics, and exhibits a frequency-dependent rise imposed by closed-
657 loop causality. The achieved total self-noise is shown for reference. (b) Comparison between the achieved total
658 self-noise and the theoretical bounds. The separation from the thermal limit quantifies the residual
659 performance gap attributable to control-loop implementation and electronic noise sources, providing a direct
660 metric to assess design margins and guide further optimization toward fundamental physical limits.



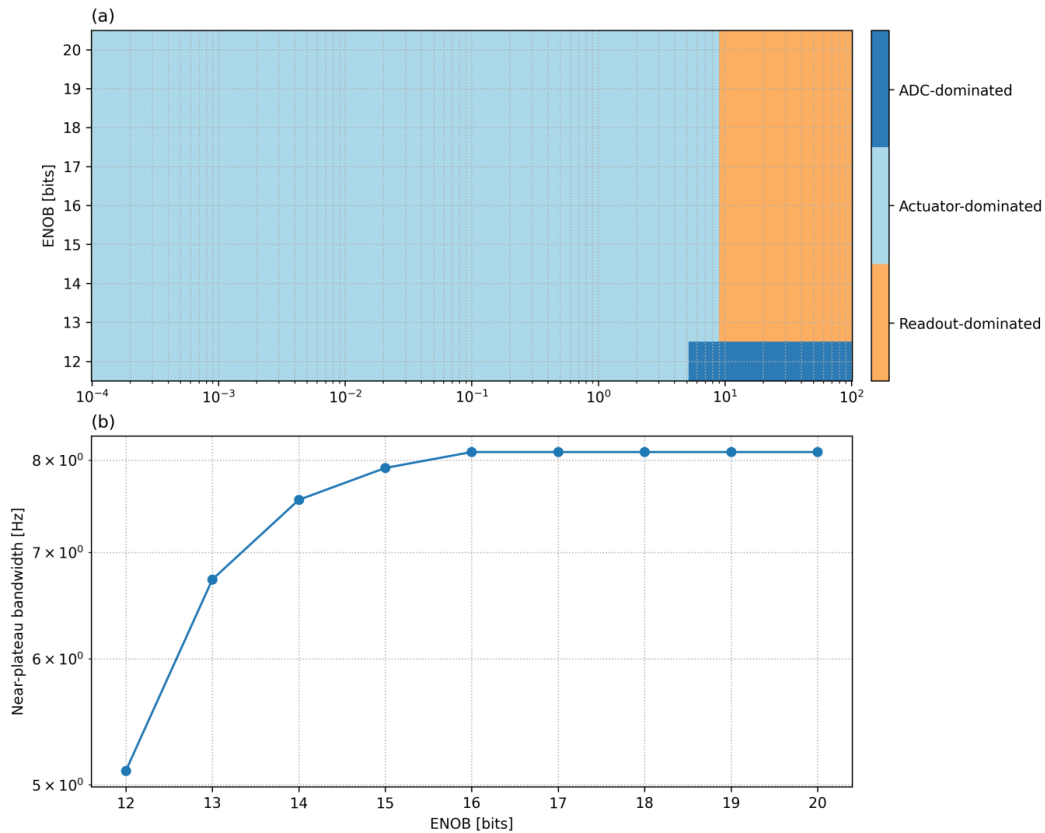
661

662 **Figure 5.** Spectral sensitivity of the closed-loop instrument self-noise to key design parameters. (a) Total
 663 acceleration self-noise amplitude spectral density $S_a^{1/2}(f)$ for different effective ADC resolutions (ENOB =
 664 12–20 bits), computed for a fixed mechanical plant ($m = 1 \text{ kg}$, $T_0 = 120 \text{ s}$, $\zeta = 0.20$) and identical control
 665 architecture. At low frequencies the spectra collapse onto a common plateau set by non-digital noise sources,
 666 whereas at higher frequencies the achievable noise floor progressively improves with increasing ENOB as
 667 quantization and digital-chain contributions are reduced. The dashed curve indicates the Brownian (thermal)
 668 acceleration limit, shown for reference. (b) Sensitivity of the total acceleration self-noise to the damping ratio
 669 $\zeta(0.05\text{--}0.30)$ at fixed ENOB (16 bits). Variations in ζ primarily affect the low-frequency noise level through the
 670 balance between thermal dissipation and feedback-related contributions, while the high-frequency rise
 671 remains controlled by the digital and readout bandwidth. The dashed line marks the nominal thermal limit.
 672 Together, the two panels illustrate how electronic resolution and mechanical damping act on distinct frequency
 673 regimes, defining complementary design trade-offs for ultra-low-frequency force-feedback inertial sensors.



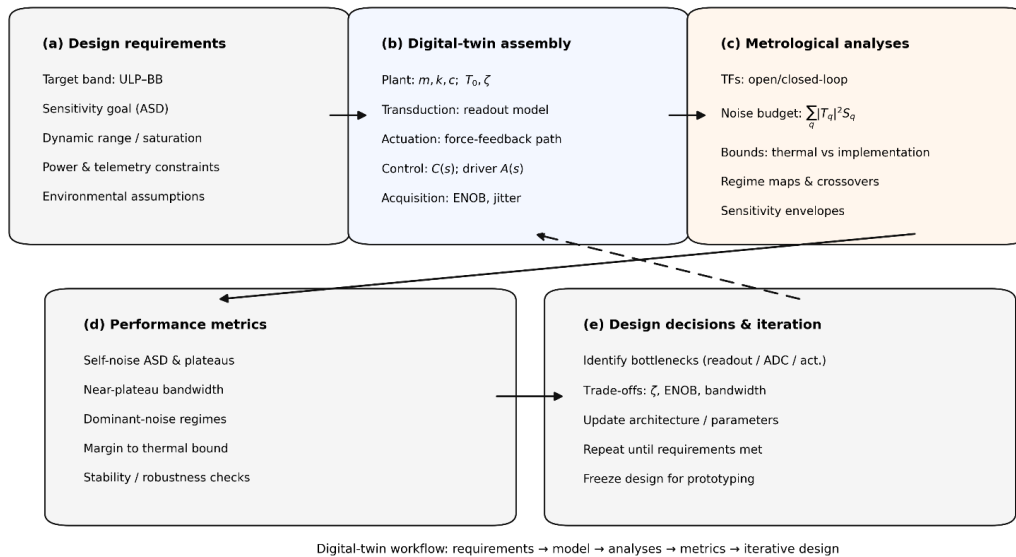
674

675 **Figure 6.** Noise regimes and crossover frequencies in a digitally controlled broadband inertial sensor. (a)
676 Acceleration noise amplitude spectral density (ASD) as a function of frequency, showing the individual
677 contributions from Brownian (thermal) noise, readout noise, actuator/feedback noise, quantization and clock
678 noise, and the digital (ADC) contribution for a nominal resolution of ENOB = 16 bits. The resulting total self-
679 noise (quadratic sum of all components) is also shown. The plot highlights the frequency-dependent dominance
680 of different noise sources, with readout noise governing the low-frequency range, actuator/feedback noise
681 setting the mid-band floor, and digital/ADC-related effects becoming relevant at higher frequencies due to
682 closed-loop shaping. (b) Crossover frequencies between selected noise contributions as a function of effective
683 ADC resolution (ENOB). The blue curve indicates the frequency at which ADC noise equals actuator/feedback
684 noise, demonstrating the systematic extension of the near-thermal bandwidth with increasing ENOB. The
685 orange curve shows the crossover between readout and actuator noise, which remains nearly invariant with
686 ENOB, reflecting its weak dependence on digitization resolution. Together, panels (a) and (b) illustrate how
687 digital resolution primarily controls the high-frequency noise budget, while low- and mid-band performance
688 are constrained by analog sensing and actuation mechanisms.



689

690 **Figure 7.** Design regime map and effective near-plateau bandwidth. (a) Dominant self-noise contributor in
691 the ENOB–frequency plane, classified by variance comparison between readout, actuator/feedback, and ADC
692 noise terms. The map highlights distinct operating regimes and shows that, for typical design parameters, the
693 system is predominantly actuator-limited over most of the seismic bandwidth, with ADC-dominated behavior
694 confined to low ENOB and high frequencies, and readout domination emerging at the highest frequencies. (b)
695 Near-plateau bandwidth as a function of ENOB, defined as the frequency range over which the total self-noise
696 remains within 30% of its minimum achievable plateau. Increasing ENOB significantly extends the usable low-
697 noise bandwidth up to $ENOB \approx 15\text{--}16$, beyond which further improvements yield diminishing returns,
698 indicating a transition to actuator/readout-limited performance. This representation provides a compact and
699 quantitative guideline for digitization requirements in force-feedback broadband sensors.



700

701 **Figure 8.** Conceptual workflow of the digital-twin framework adopted for the engineering design and
 702 metrological assessment of ultra-low-noise broadband inertial sensors. (a) Definition of design requirements,
 703 including target bandwidth, sensitivity objectives, dynamic range constraints, and environmental assumptions.
 704 (b) Assembly of the digital twin, integrating the mechanical plant, transduction chain, force-feedback
 705 actuation, control architecture, and acquisition system. (c) Metrological analyses performed in the frequency
 706 domain, encompassing open- and closed-loop transfer functions, full noise-budget decomposition, and
 707 theoretical versus implementation-dependent performance bounds. (d) Extraction of performance metrics,
 708 such as self-noise plateaus, near-plateau bandwidth, dominant noise regimes, and margins relative to the
 709 thermal limit. (e) Iterative design loop, where identified bottlenecks guide trade-offs among damping, ENOB,
 710 and bandwidth, leading to progressive architectural refinement and final design freeze. Solid arrows indicate
 711 the nominal forward workflow, whereas the dashed arrow highlights the feedback loop driving iterative
 712 optimization.